Geophysical Research Letters

Supporting Information for

Fossil vs. non-fossil CO sources in the US: New airborne constraints from ACT-America and GEM

Andres Gonzalez[1], Dylan B. Millet[1], Xueying Yu[1], Kelley C. Wells[1], Timothy J. Griffis[1], Bianca C. Baier[2,3], Patrick C. Campbell[4,5,6], Yonghoon Choi[7], Joshua P. DiGangi[7], Alexander Gvakharia[8], Hannah S. Halliday[7], Eric A. Kort[8], Kathryn McKain[2,3], John B. Nowak[6], and Genevieve Plant[8]

[1]Department of Soil, Water, and Climate, University of Minnesota, Saint Paul, MN, USA. [2]Cooperative Institute for Research in Environmental Sciences (CIRES), University of Colorado, Boulder, CO, USA. [3]Global Monitoring Laboratory, National Oceanic and Atmospheric Administration, Boulder, CO, USA. [4]Center for Spatial Information Science and Systems, George Mason University, Fairfax, VA, USA. [5]Cooperative Institute for Satellite Earth System Studies (CISESS), College Park, MD, USA. [6]Air Resources Laboratory, National Oceanic and Atmospheric Administration, College Park, MD, USA. [7]NASA Langley Research Center, Hampton, VA, USA. [8]Department of Climate and Space Sciences and Engineering, University of Michigan, Ann Arbor, MI, USA.
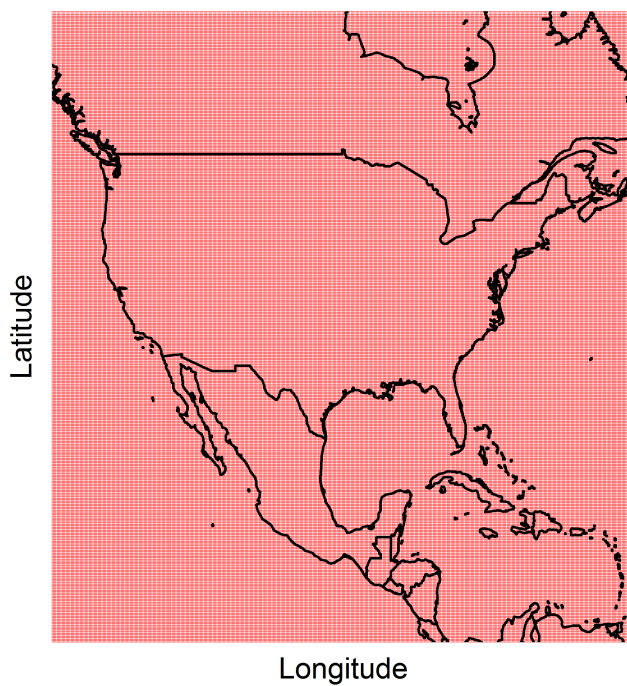
Contents of this file
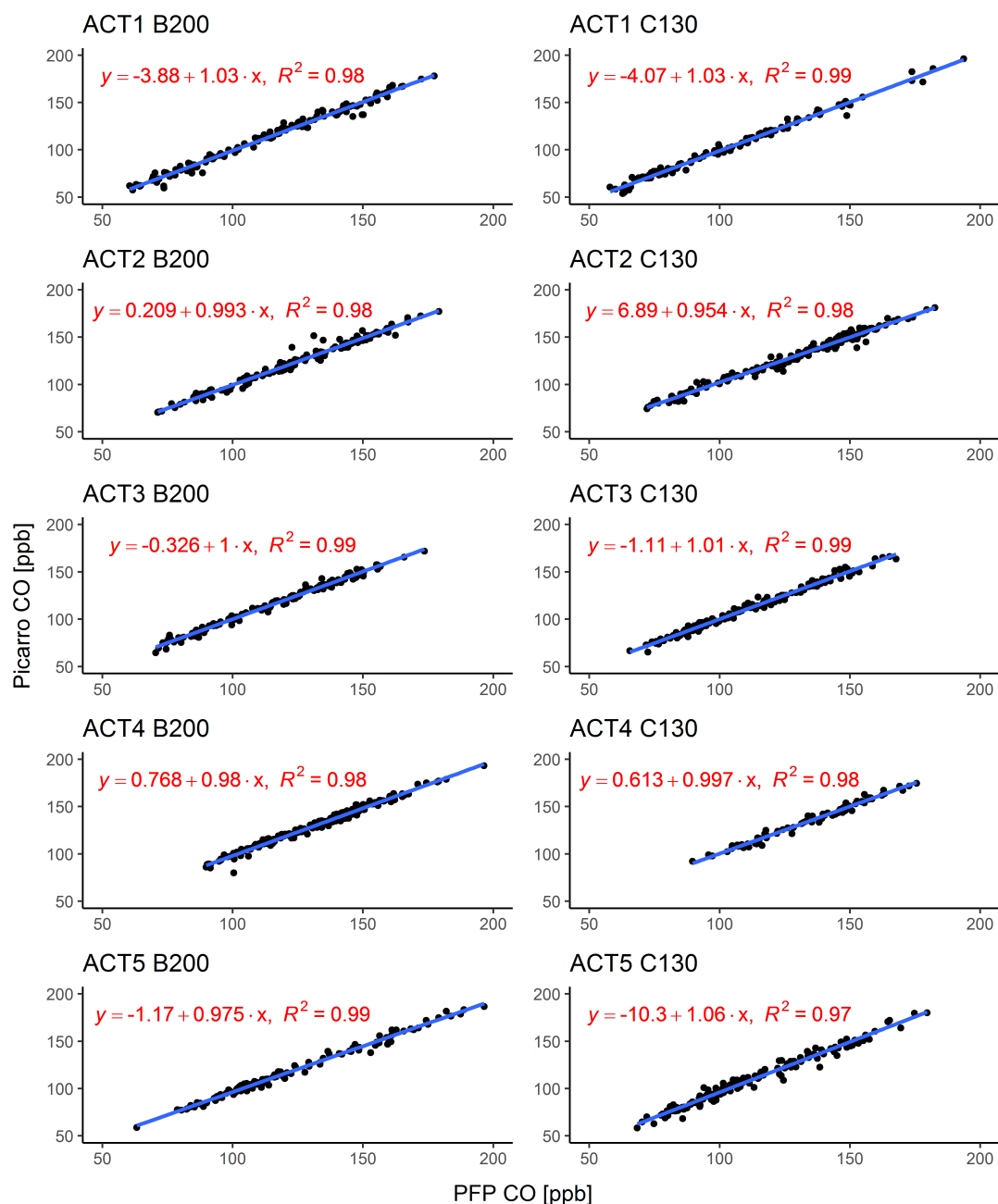
Figure S1. Intercomparison of ACT-America airborne CO measurements. In situ measurements by Picarro CRDS are plotted against PFP flask measurements on-board the Beechcraft B200 King Air (left column) and C-130H Hercules (right column) aircraft for each ACT-America deployment.

Figure S2. North American nested domain employed for GEOS-Chem simulations.
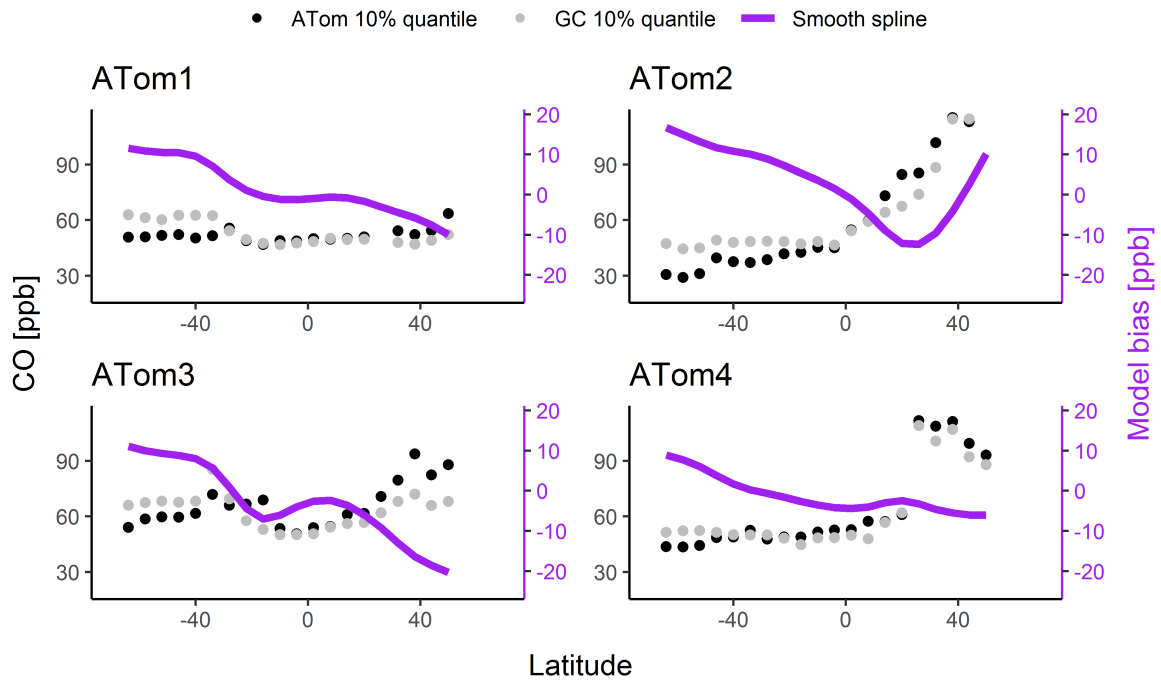
Figure S3. Correction of the GEOS-Chem CO background based on aircraft measurements from the four ATom deployments. Plotted are observed tropospheric CO mixing ratios over the remote Pacific Ocean averaged by six-degree latitude bins (black) along with the corresponding model values (grey). Data shown are restricted to 0-8 km above sea level, 80°S-56°N, and 160°E-145°W (Northern Hemisphere) or 100°W-145°W (Southern Hemisphere). Purple lines show the model-measurement mismatch as a smooth spline fit to the 0.1 quantile difference.
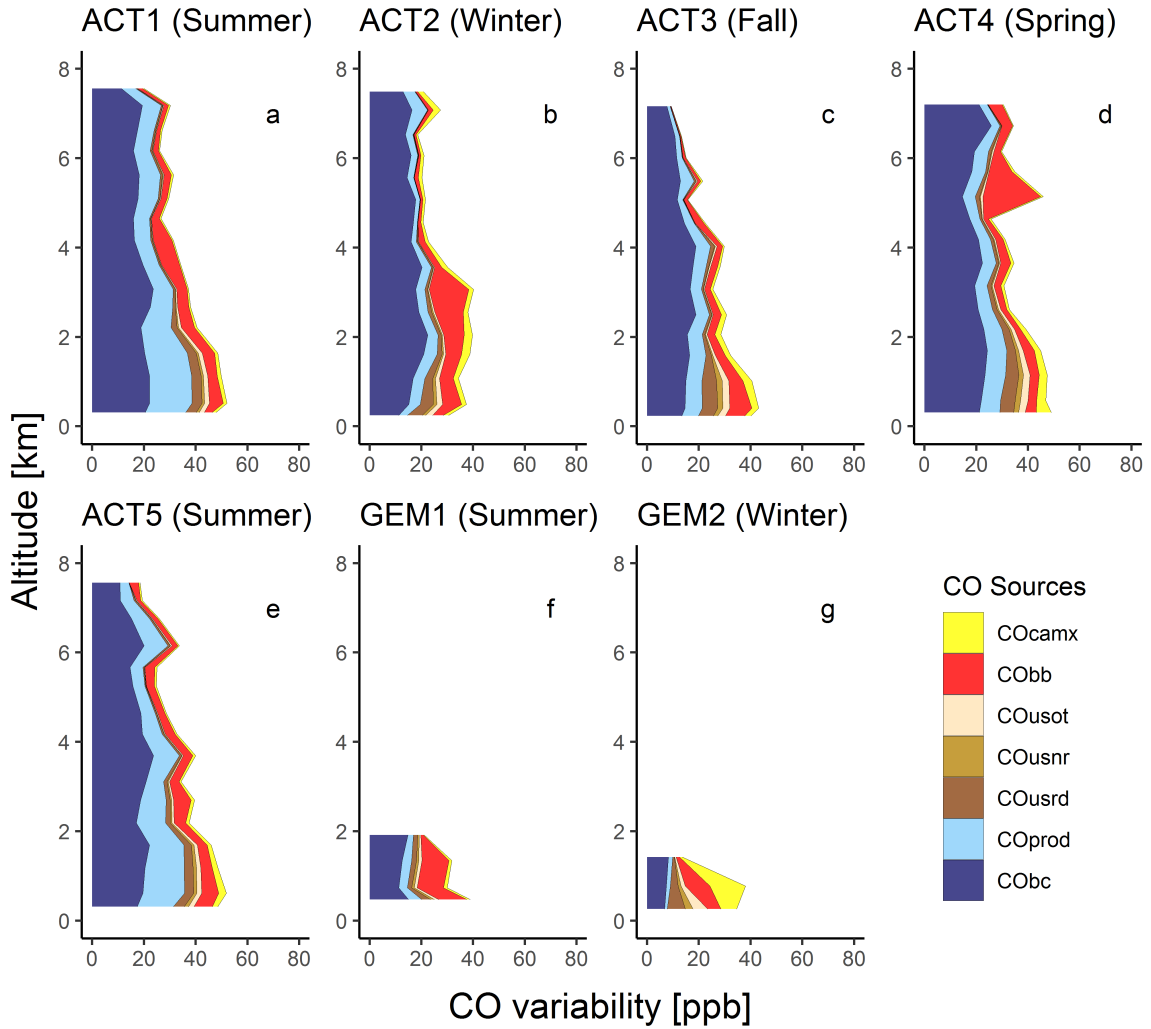
Figure S4. Sources of CO variability over the eastern US. Plotted is the standard deviation for individual tagged CO tracers based on output from the optimized GEOS-Chem simulation along the ACT-America and GEM flight tracks. CO_{bc}: CO transported from outside North America. CO_{usrd}, CO_{usnr}, CO_{usot}: anthropogenic CO emitted from US on-road, non-road, and other sources. CO_{camx}: anthropogenic CO emitted in Canada + Mexico. CO_{bb}: CO emitted from North American biomass burning. CO_{prod}: CO photochemically produced over North America. Standard deviation is not additive so the individual values do not sum to the total CO variability.
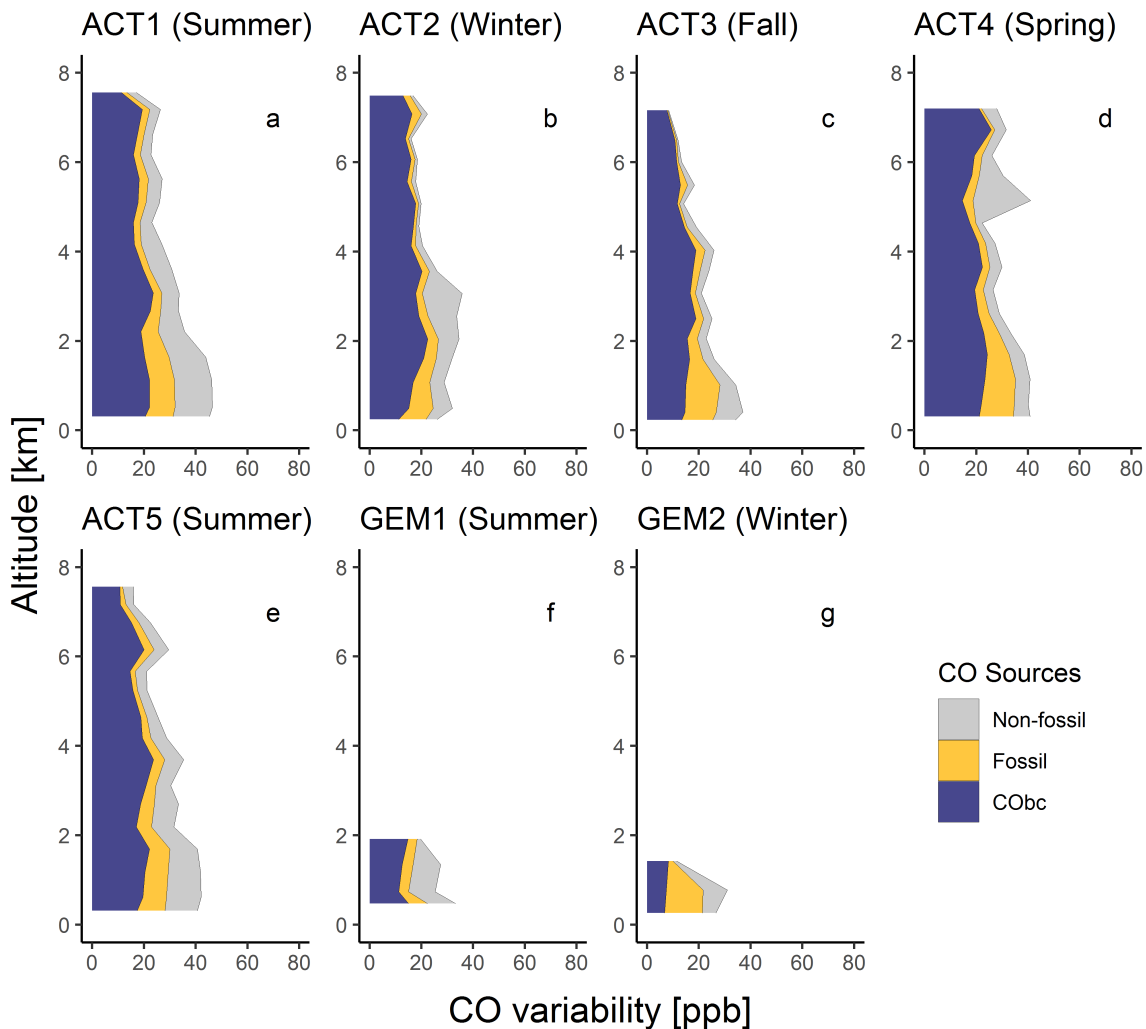
Figure S5. Sources of CO variability over the eastern US. Plotted is the standard deviation for grouped tagged CO tracers from the optimized GEOS-Chem simulation along the ACT-America and GEM flight tracks. Values are shown for non-fossil CO (from biogenic VOC oxidation plus biomass burning emissions), fossil CO (from direct emissions plus anthropogenic VOC oxidation), and CO transported from outside North America (CO_{bc}). Standard deviation is not additive so the individual values do not sum to the total CO variability.

ACT1 SD Summer

Background

Biomass Burning

Secondary Production

Direct Fossil

CO [ppb]
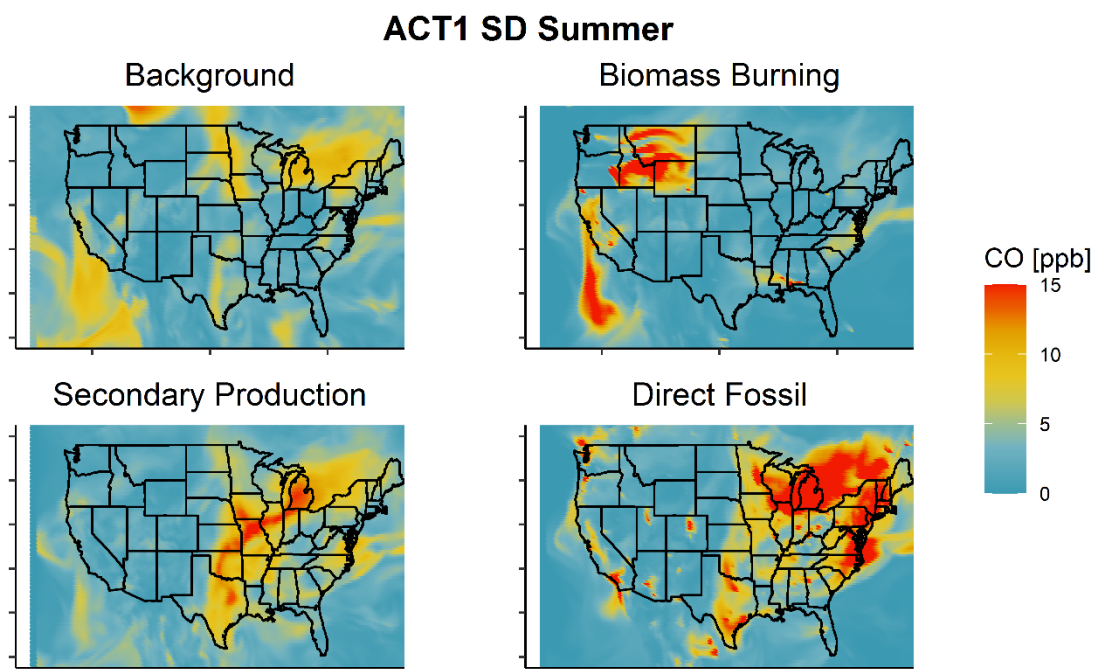
Figure S6. Temporal CO variability in the US PBL during summer. Plotted are the hourly standard deviations (SD) for background CO, biomass burning CO, secondary CO, and directly-emitted fossil fuel CO based on the optimized GEOS-Chem simulation. Data are plotted for the ACT1 timeframe (11 July to 29 August 2016).

ACT2 SD Winter
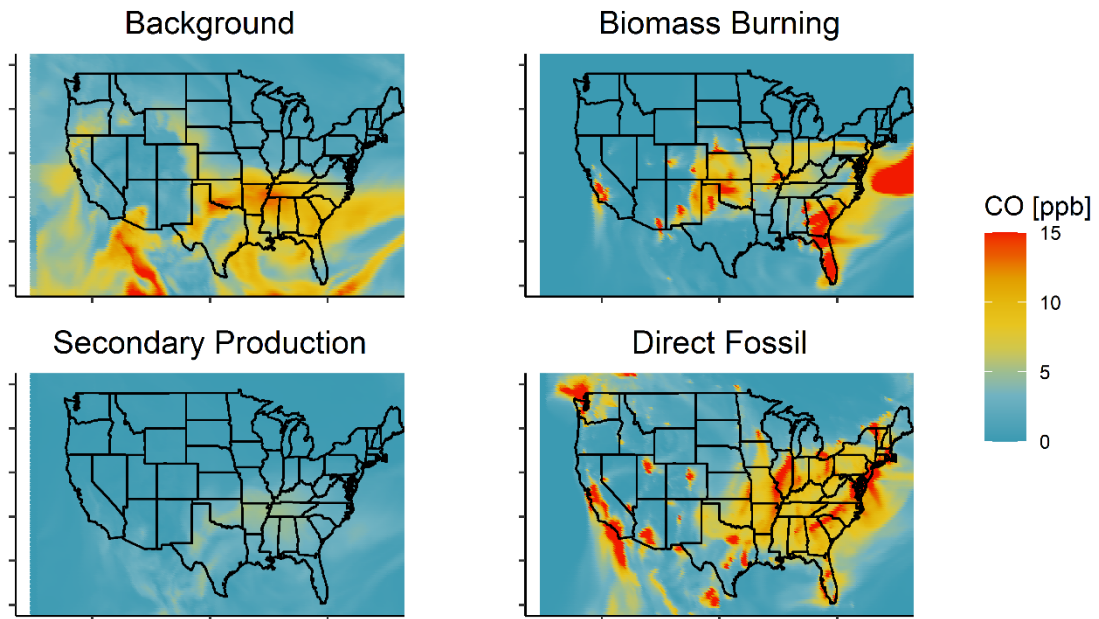
Figure S7. Temporal CO variability in the US PBL during winter. Plotted are the hourly standard deviations (SD) for background CO, biomass burning CO, secondary CO, and directly-emitted fossil fuel CO based on the optimized GEOS-Chem simulation. Data are plotted for the ACT2 timeframe (21 January to 10 March 2017).

ACT3 SD Fall

Figure S8. Temporal CO variability in the US PBL during fall. Plotted are the hourly standard deviations (SD) for background CO, biomass burning CO, secondary CO, and directly-emitted fossil fuel CO based on the optimized GEOS-Chem simulation. Data are plotted for the ACT3 timeframe (22 September to 13 November 2017).
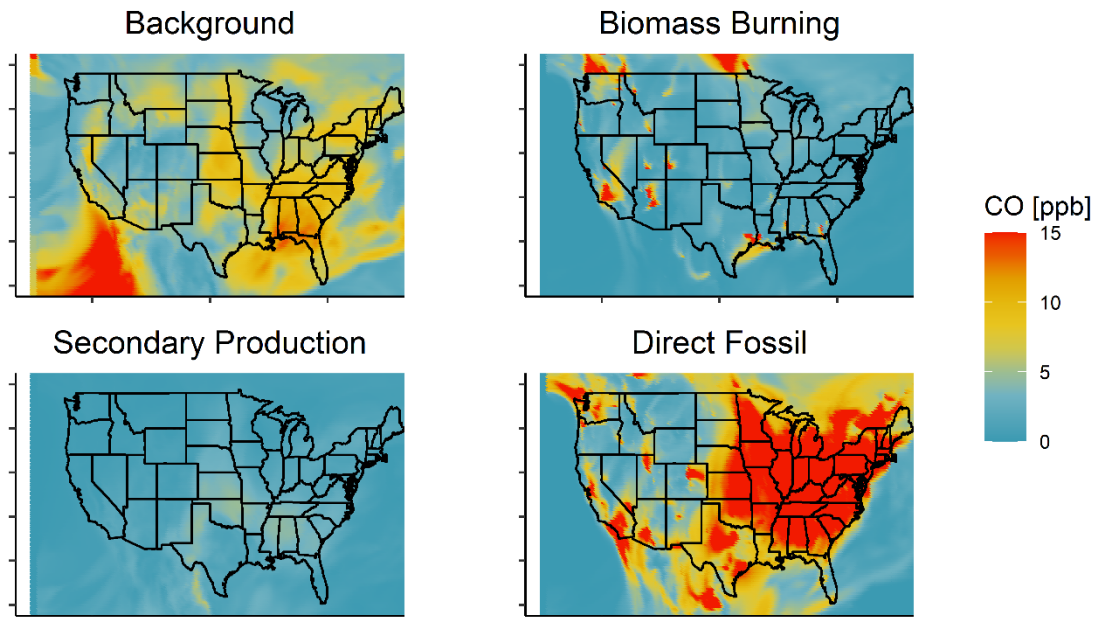
ACT4 SD Spring

Figure S9. Temporal CO variability in the US PBL during spring. Plotted are the hourly standard deviations (SD) for background CO, biomass burning CO, secondary CO, and directly-emitted fossil fuel CO based on the optimized GEOS-Chem simulation. Data are plotted for the ACT4 timeframe (28 March to 20 May 2018).
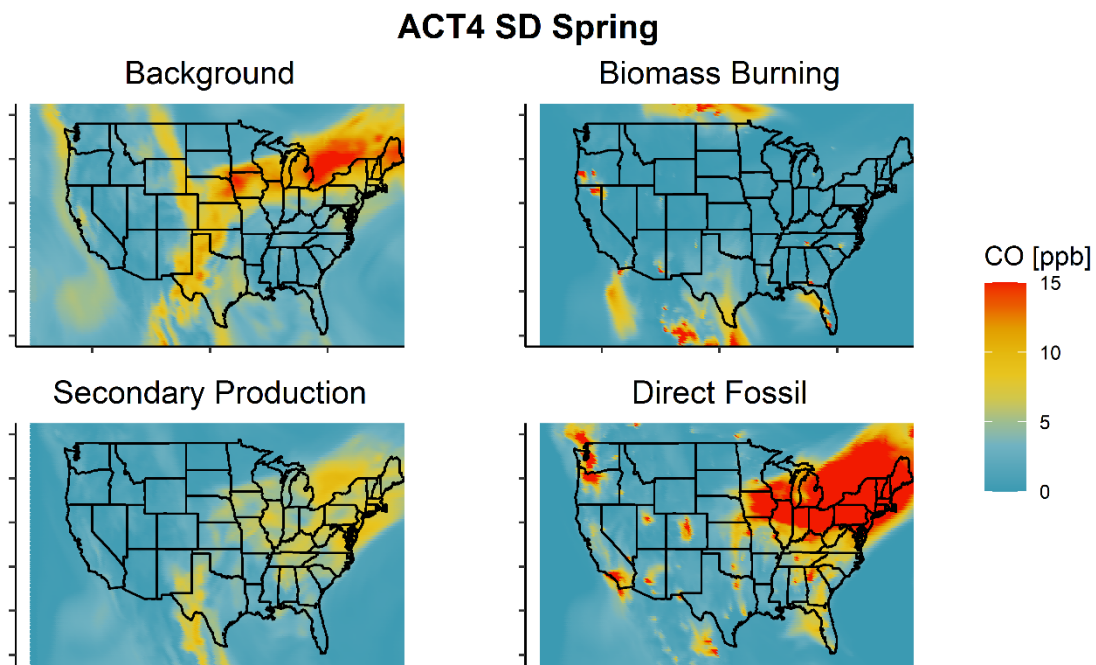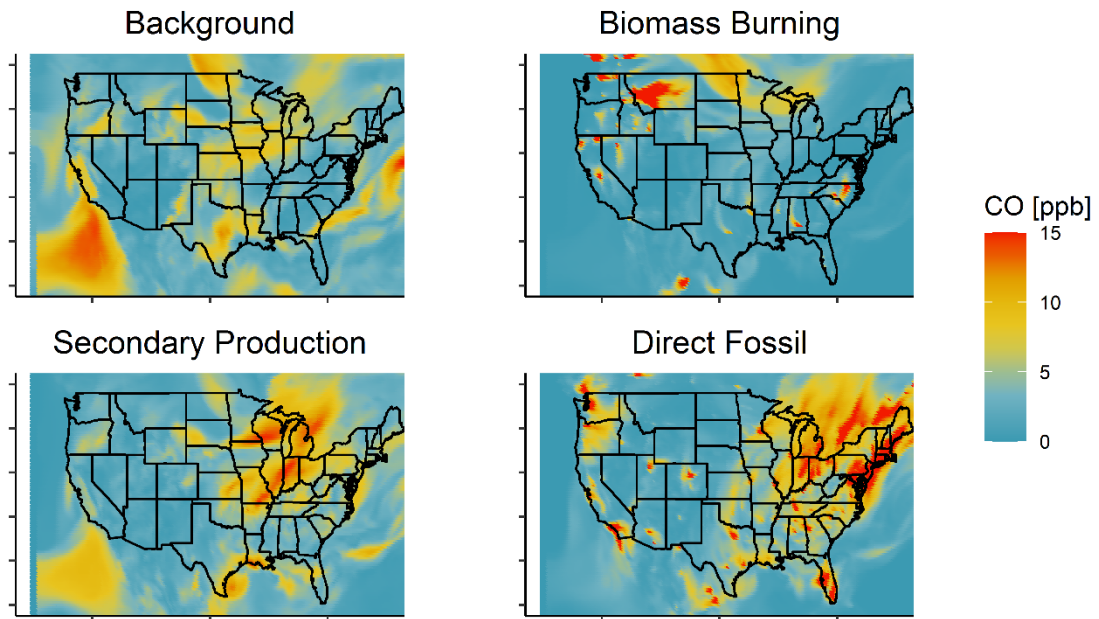
ACT5 SD Summer

Figure S10. Temporal CO variability in the US PBL during summer. Plotted are the hourly standard deviations (SD) for background CO, biomass burning CO, secondary CO, and directly-emitted fossil fuel CO based on the optimized GEOS-Chem simulation. Data are plotted for the ACT5 timeframe (7 June to 27 July 2019).

ACT1 Mean Summer

Background

Biomass Burning

Secondary Production
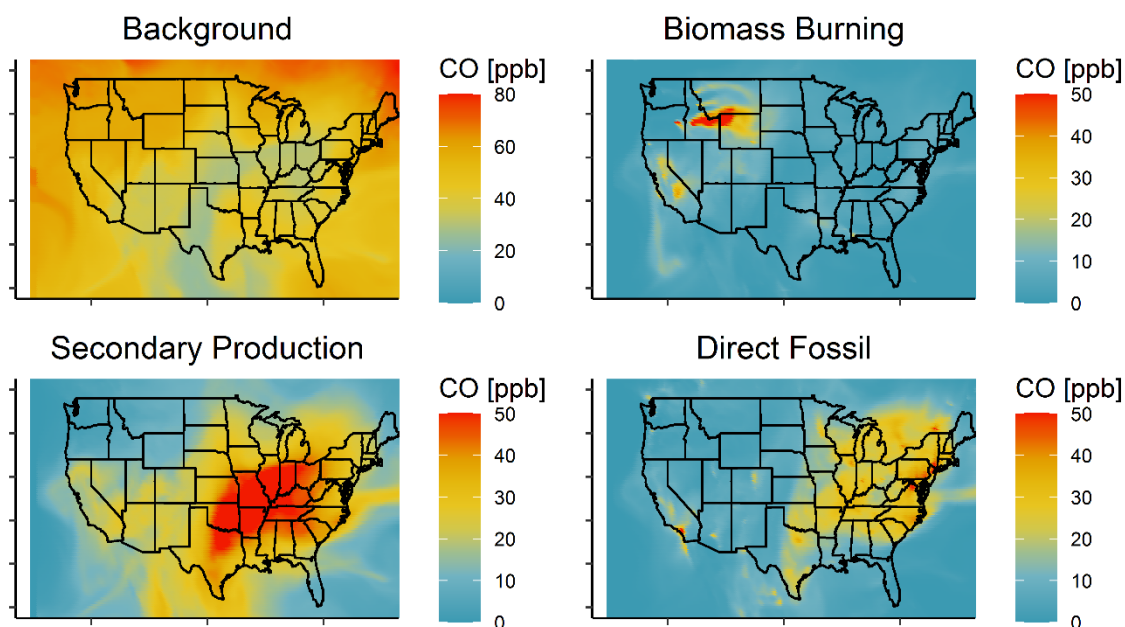
Direct Fossil

Figure S11. Contributions to the PBL CO burden over the US during summer. Plotted are the mean contributions from background CO, direct biomass burning emissions, secondary production, and direct fossil fuel emissions based on the optimized GEOS-Chem simulation. Data are plotted for the ACT1 timeframe (11 July to 29 August 2016).

ACT2 Mean Winter

Background

Biomass Burning

Secondary Production
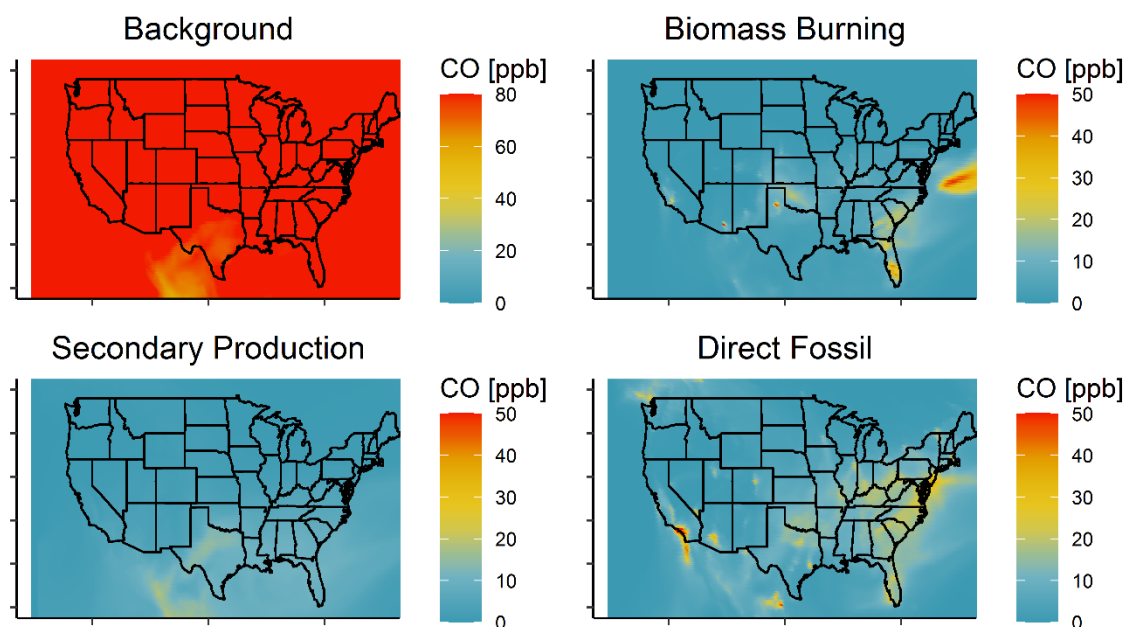
Direct Fossil

Figure S12. Contributions to the PBL CO burden over the US during winter. Plotted are the mean contributions from background CO, direct biomass burning emissions, secondary production, and direct fossil fuel emissions based on the optimized GEOS-Chem simulation. Data are plotted for the ACT2 timeframe (21 January to 10 March 2017).

Figure S13. Contributions to the PBL CO burden over the US during fall. Plotted are the mean contributions from background CO, direct biomass burning emissions, secondary production, and direct fossil fuel emissions based on the optimized GEOS-Chem simulation. Data are plotted for the ACT3 timeframe (22 September to 13 November 2017).
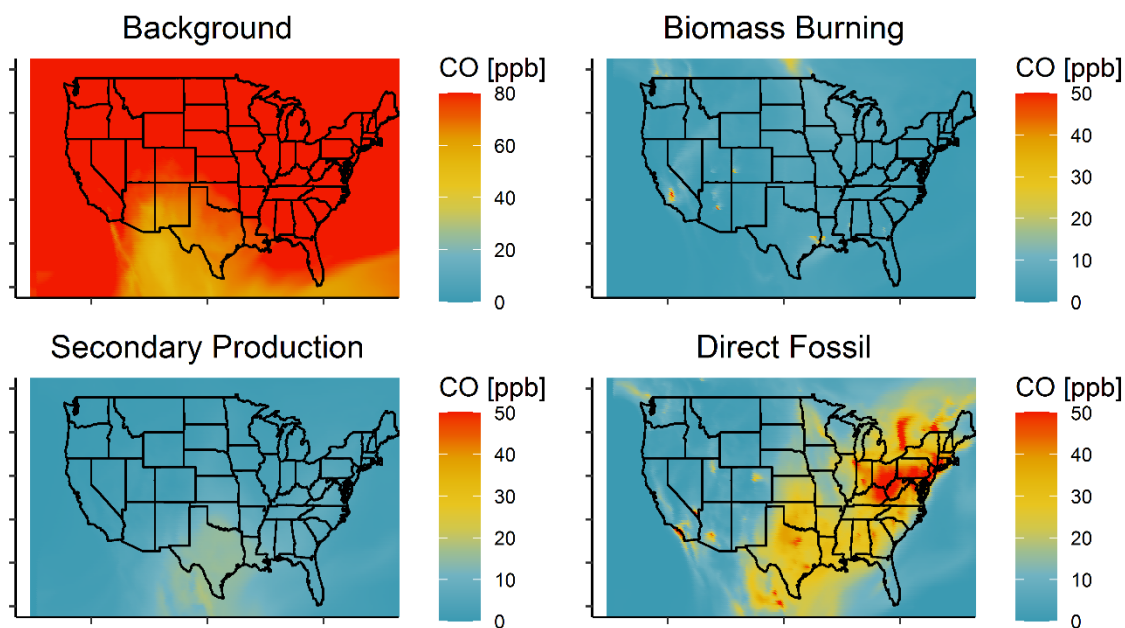
Figure S14. Contributions to the PBL CO burden over the US during spring. Plotted are the mean contributions from background CO, direct biomass burning emissions, secondary production, and direct fossil fuel emissions based on the optimized GEOS-Chem simulation. Data are plotted for the ACT4 timeframe (28 March to 20 May 2018).
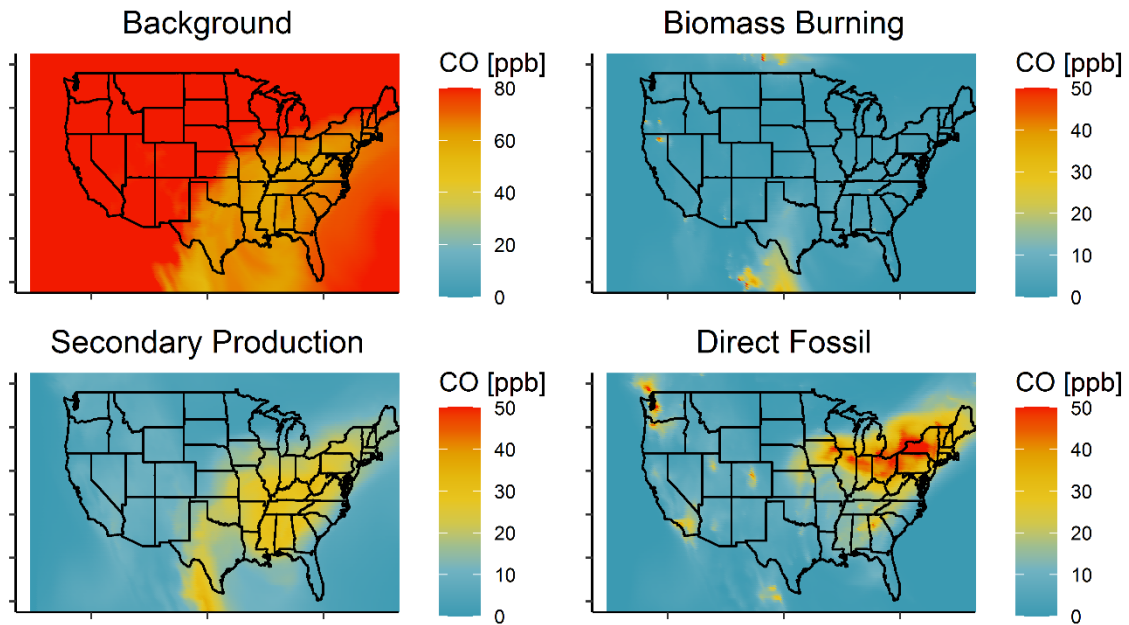
ACT5 Mean Summer
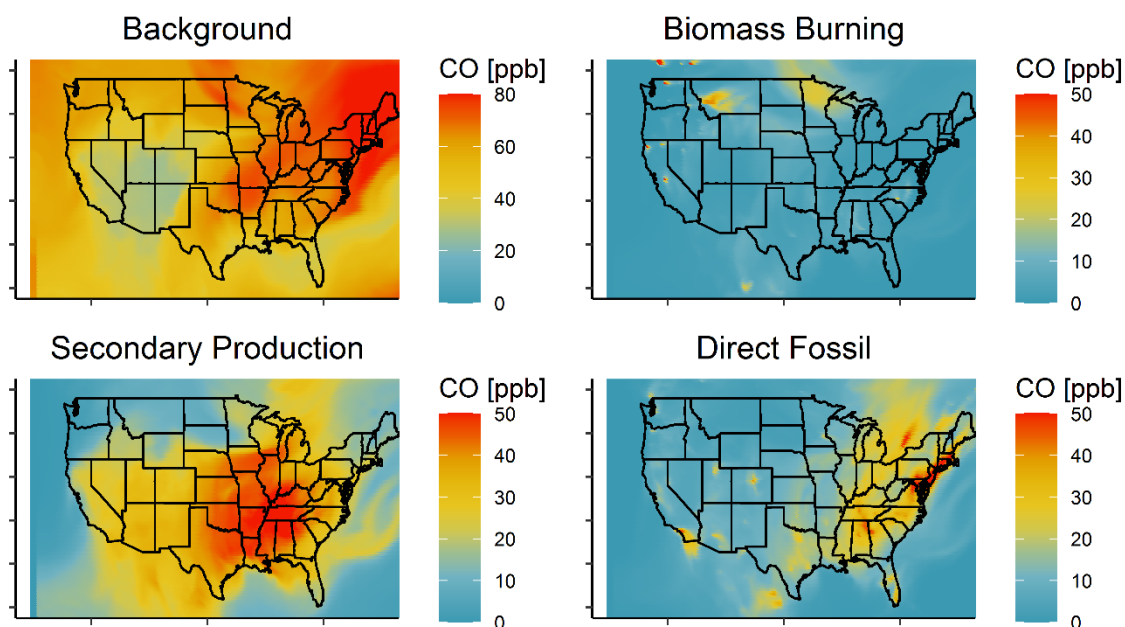
Figure S15. Contributions to the PBL CO burden over the US during summer. Plotted are the mean contributions from background CO, direct biomass burning emissions, secondary production, and direct fossil fuel emissions based on the optimized GEOS-Chem simulation. Data are plotted for the ACT5 timeframe (7 June to 27 July 2019).
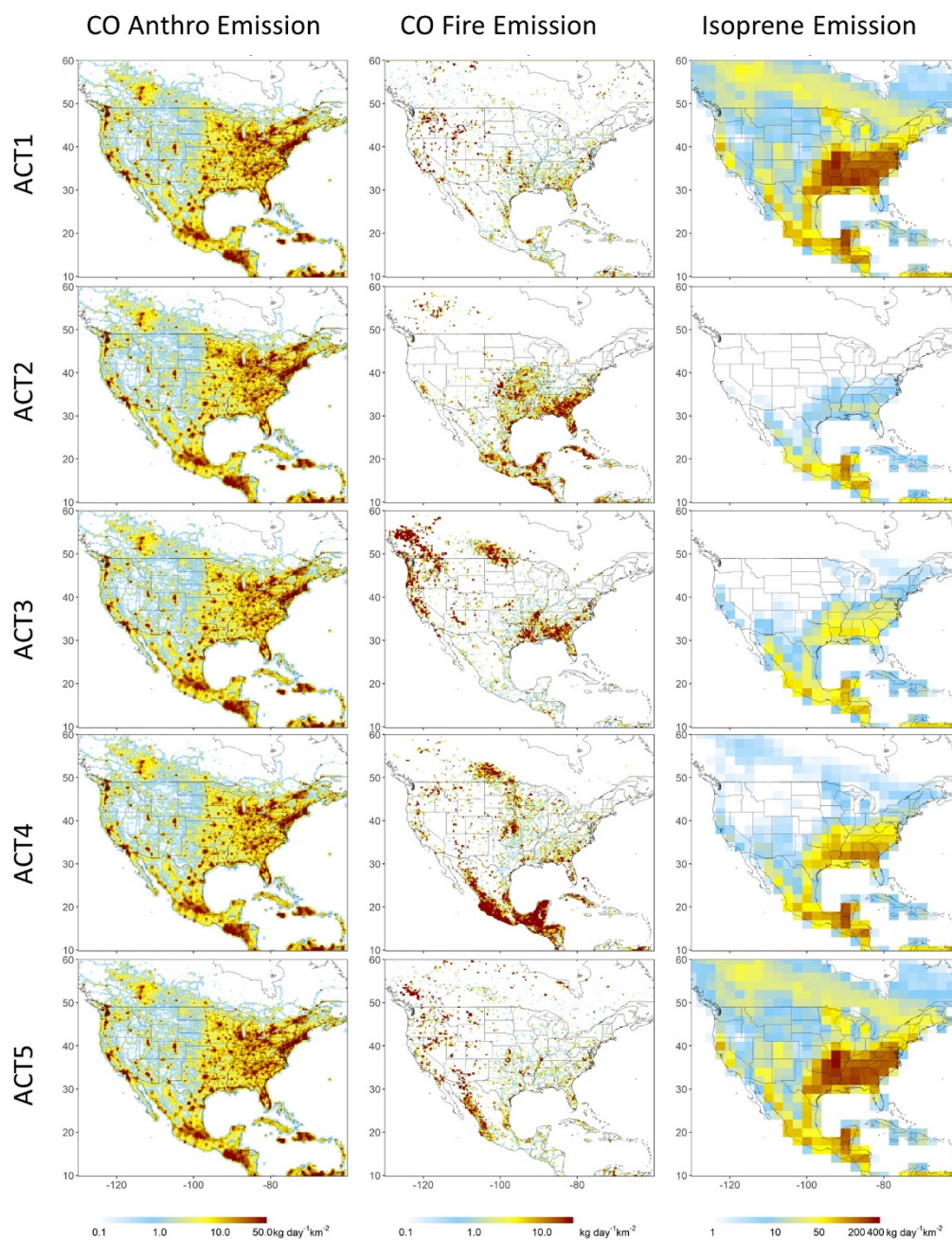
Figure S16. North American CO sources based on the prior inventories employed in this work. Left column: CO directly emitted from anthropogenic sources. Middle column: CO emitted from open burning. Right column: biogenic emissions of isoprene, a key CO precursor.

Table S1. Timeframe and flight hours for the ACT-America and GEM airborne campaigns.

Campaign	Year	Season	Start Date	End Date	Flight Hours
ACT1	2016	Summer	11 July	29 August	218
ACT2	2017	Winter	21 January	10 March	210
ACT3	2017	Fall	22 September	13 November	192
ACT4	2018	Spring	28 March	20 May	197
ACT5	2019	Summer	7 June	27 July	183
GEM1	2017	Summer	12 August	24 August	40
GEM2	2018	Winter	17 January	28 January	36

Table S2. Statistical comparison of CO mixing ratios from the prior and optimized GEOS-Chem simulations against independent airborne observations from the ACT5, GEM1, and GEM2 campaigns.

	RMSE[1] (ppb)		R		Mean Bias (ppb)[2]	
	Prior	Post	Prior	Post	Prior	Post
ACT5 (summer)	28.2	23.2	0.51	0.57	-14.0	-7.8
GEM1 (summer)	57.8	35.8	0.23	0.06	-48.4	-12.5
GEM2 (winter)	60.9	59.1	0.36	0.32	-21.9	-11.8

[1] Root mean square error.
[2] Mean of simulated minus observed values.

Table S3. Seasonal CO source optimization performed separately for the C-130H and B200 ACT-America datasets.

		CO_{usnei}		CO_{prod_voc}				RMSE (ppb)[3]		R		Mean Bias[4]	
	Aircraft	**Scale factor**	**Mean (ppb)**	**Scale factor**	**Mean (ppb)**	**Intercept**	**VIF[2]**	**Prior**	**Post**	**Prior**	**Post**	**Prior**	**Post**
ACT1 (summer)	B200	0.54 ± 0.05[1]	13.1	0.96 ± 0.02	25.4	0.09 ± 0.3	3.37	26.2	16.2	0.76	0.81	-17.7	-0.4
	C-130H	0.87 ± 0.09	13.4	0.74 ± 0.02	25.3	8.28 ± 0.3	2.74	26.6	17.3	0.74	0.80	-17.4	-2.1
ACT2 (winter)	B200	0.86 ± 0.04	13.4			0.43 ± 0.4 4		21.7	16.7	0.66	0.65	-14.3	-0.4
	C-130H	0.67 ± 0.04	11.8			5.5 ± 0.48		21.0	13.7	0.75	0.77	-16.0	-3.8
ACT3 (fall)	B200	0.65 ± 0.04	17.5			6.4 ± 0.6		13.6	14.4	0.79	0.75	-2.1	-6.1
	C-130H	0.79 ± 0.03	15.7			4.2 ± 0.41		13.0	13.6	0.79	0.76	-3.2	-4.2
ACT4 (spring)	B200	0.76 ± 0.02	15.6			-4.5 ± 0.44		17.8	17.5	0.63	0.59	-7.8	4.4
	C-130H	0.65 ± 0.03	20.29			2.61 ± 0.61		18.8	16.0	0.71	0.68	-11.3	-2.8

[1] Stated uncertainties reflect 95% confidence intervals computed through bootstrap resampling.
[2] Variance inflation factor.
[3] Root mean square error.
[4] Mean of simulated minus observed values.

Table S4. Seasonal CO source optimization performed with and without ATom-based boundary condition correction.

	CO_{bc}	CO_{usnei} Scale factor	CO_{usnei} Mean (ppb)	CO_{prod_voc} Scale factor	CO_{prod_voc} Mean (ppb)	Intercept	VIF[2]	RMSE (ppb)[3] Prior	RMSE (ppb)[3] Post	R Prior	R Post	Mean Bias[4] Prior	Mean Bias[4] Post
ACT1 (summer)	Corrected	0.66 ± 0.05[1]	13.2	0.91 ± 0.03	25.4	-0.2 ± 0.3	3.1	26.4	16.8	0.75	0.81	-17.6	2.5
	Uncorrected	0.69 ± 0.05	13.22	0.85 ± 0.02	25.4	2.7 ± 0.3	2.1	26.4	17.0	0.75	0.80	-11.7	1.2
ACT2 (winter)	Corrected	0.79 ± 0.03	12.77			1.8 ± 0.4		21.4	15.5	0.69	0.69	-14.8	-1.7
	Uncorrected	0.85 ± 0.03	12.77			-4.3 ± 0.3		21.4	15.5	0.69	0.74	-14.8	4.2
ACT3 (fall)	Corrected	0.69 ± 0.03	16.77			5.5 ± 0.5		13.4	14.2	0.79	0.75	-2.5	-5.5
	Uncorrected	0.66 ± 0.03	16.77			6.7 ± 0.5		13.4	14.7	0.79	0.75	-2.6	-6.7
ACT4 (spring)	Corrected	0.74 ± 0.02	16.94			-2.7 ± 0.4		18.1	17.0	0.65	0.61	-8.8	2.6
	Uncorrected	0.75 ± 0.02	16.94			-3.2 ± 0.4		18.1	17.2	0.65	0.60	-8.8	3.0

[1] Stated uncertainties reflect 95% confidence intervals computed through bootstrap resampling
[2] Variance inflation factor.
[3] Root mean square error.
[4] Mean of simulated minus observed values.

Table S5. Seasonal CO source optimization for ACT1-ACT4 with alternative tracer groupings: 1) CO_{usnei} and 2) the sum of all other regional source tracers ($CO_{prod\_voc} + CO_{camx} + CO_{bb}$).

	CO_{usnei}		$CO_{prod\_voc} + CO_{camx} + CO_{bb}$		Intercept	VIF[2]	RMSE[3] (ppb)		R		Mean Bias[4]	
	Scale factor	Mean (ppb)	Scale factor	Mean (ppb)			Prior	Post	Prior	Post	Prior	Post
ACT1 (summer)	0.58 ± 0.05[1]	13.2	0.96 ± 0.02	26.7	-0.4 ± 0.3	2.9	26.4	16.6	0.75	0.81	-17.6	0.3
ACT2 (winter)	0.85 ± 0.03	12.77	0.7 ± 0.07	7.1	3.1 ± 0.5	1.1	21.4	15.6	0.69	0.70	-14.8	-3.1
ACT3 (fall)	0.82 ± 0.03	16.77	0.55 ± 0.01	14.6	5.5 ± 0.5	1.2	13.4	15.9	0.79	0.76	-2.5	-10.1
ACT4 (spring)	0.70 ± 0.02	16.94	1.1 ± 0.05	12.6	-3.6 ± 0.5	1.4	18.1	17.2	0.65	0.61	-8.8	3.6

[1] Stated uncertainties reflect 95% confidence intervals computed through bootstrap resampling

[2] Variance inflation factor.

[3] Root mean square error.

[4] Mean of simulated minus observed values.